A Parameter–Free Generalized Moment Limiter for High-Order Methods on Unstructured Grids

Michael Yang[1] and Z.J. Wang[1,*]

[1] *Department of Aerospace Engineering and CFD Center, Iowa State University, Ames, IA 50011, USA*

Abstract. A parameter-free limiting technique is developed for high-order unstructured-grid methods to capture discontinuities when solving hyperbolic conservation laws. The technique is based on a "troubled-cell" approach, in which cells requiring limiting are first marked, and then a limiter is applied to these marked cells. A parameter-free accuracy-preserving TVD marker based on the cell-averaged solutions and solution derivatives in a local stencil is compared to several other markers in the literature in identifying "troubled cells". This marker is shown to be reliable and efficient to consistently mark the discontinuities. Then a compact high-order hierarchical moment limiter is developed for arbitrary unstructured grids. The limiter preserves a degree p polynomial on an arbitrary mesh. As a result, the solution accuracy near smooth local extrema is preserved. Numerical results for the high-order spectral difference methods are provided to illustrate the accuracy, effectiveness, and robustness of the present limiting technique.

AMS subject classifications: 65M70, 76M20, 76M22

Key words: Limiter, shock-capturing, high-order, unstructured grids.

1 Introduction

A nonlinear hyperbolic conservation law can generate discontinuities even if the initial solution is smooth. A significant computational challenge with a nonlinear hyperbolic conservation law is the resolution of such discontinuities, which has been a very active area of research for over four decades. However, any linear scheme higher than first order accuracy cannot generate monotonic solutions, according to the Godunov theorem [8]. This means linear schemes of 2nd-order and higher will produce spurious oscillations near discontinuities due to the so-called Gibbs phenomenon, which can result in numerical instability and non-physical data, such as negative pressure

---

or density. Early research work on shock-capturing relied on numerical diffusion to smear the discontinuities so that they can be captured as part of the numerical solution [14, 20, 25, 40]. Besides the existence of user-defined parameters, the historical drawback of the artificial viscosity approach is that the added terms are frequently too dissipative in certain regions of the flow. Later, another type of approach was developed based on flux limiting, which introduced numerical diffusion implicitly to reduce or remove spurious oscillations. Pioneering works in flux limiting include the FCT [3], the MUSCL and related methods [9, 38, 39], and TVD methods [10, 44]. However, the flux-limiting and TVD methods suffered from accuracy-degradation to first-order at local extrema in smooth regions.

High-order (3rd-order and higher) shock-capturing algorithms have the potential to obtain sharp non-oscillatory shock profile and simultaneously preserve accuracy in smooth regions. The challenge of producing oscillation-free numerical solutions is tougher for high-order methods than for lower order ones because of much reduced numerical dissipation. The artificial viscosity method has been improved [6, 7, 36] to minimize undesirable dissipation by using a spectrally vanishing viscosity approach based on high-order derivatives of the strain rate tensor, though there still exist user-defined parameters that can be mesh or problem dependent. The ENO [9] and WENO methods [15] used the idea of adaptive stencils in the reconstruction procedure based on the smoothness of the local numerical solution. However, due to a lack of compactness, the implementation of both ENO and WENO methods is complicated on arbitrary unstructured meshes, especially for 3D problems.

High-order methods designed for unstructured meshes offer obvious advantages in geometric flexibility. Examples of such methods include the discontinuous Galerkin (DG) method [4, 5, 30], the multi-domain staggered- grid method [16, 17], the spectral volume method [41, 42], the spectral difference (SD) method [22, 34]. A review of these and other unstructured-grid based high-order methods can be found in [43]. These high-order methods are usually compact, meaning cells are coupled with their immediate face neighbors. Compact high-order methods are much more suitable for massively parallel machines as the amount of data communication is minimized. In designing limiters for such methods, it is natural to require that the limiters should be compact. There have been many notable developments in limiters for high-order methods in the last decade. Many of the limiters employ the so-called "troubled cell" (TC) approach, in which "oscillatory" cells are marked first, and the solutions in these cells are re-generated to remove or reduce the oscillations satisfying certain criteria such as mean-preserving. The idea is first developed in [5], and then further extended in [2]. In [5], a limiter developed for the finite volume method [1] was used. The moment limiter developed in [2] can be viewed as the generalization of the minmod limiter [39] to higher order derivatives or moments. The central DG scheme proposed in [23] is a further generalization of the MUSCL scheme and the moment limiter. Other more recent developments include the use of WENO [28] and Hermite WENO [24, 29] schemes to generate the reconstruction in "troubled cells". High-order limiters based on artificial viscosity have also been investigated by various researchers [13,26]. In the

present study, our focus is on the TC approach.

There are two major components in the TC approach: the marking or detection of "troubled cells", and the data limiting (or remapping) in these cells. In developing the present moment-based limiter, we set to achieve several goals: (1) free of user adjustable parameters; (2) capable of preserving accuracy at smooth regions including smooth extrema; (3) compact and efficient for arbitrary unstructured meshes. The requirement of no-user adjustable parameters is very important for a general purpose production-type flow solver, which can be applied to a wide variety of problems. If a limiter's success hinges on a "suitable" parameter which depends on the solution, the mesh and the order of accuracy, the limiter will more likely fail than succeed in real world applications. In the present study, we compare several markers investigated in [27], namely, the minmod TVB marker [5], the KXRCF marker developed by Krivodonova et al. in [19], and the Harten marker [11], with a parameter-free accuracy-preserving TVD marker. For the limiter step, we extend the approach in [2] and [23] to arbitrary unstructured meshes in an efficient manner. Numerical results show that the present limiter can preserve accuracy at smooth regions, while capturing discontinuities.

The remainder of this paper is organized as follows. In Section 2 we review the formulation of the spectral difference method as it will be used as the carrier of the present limiter. In Section 3 we compare several markers in the literature and describe in detail the construction and implementation of the present TVD marker. In Section 4, we formulate the generalized moment limiter for arbitrary unstructured meshes. In Section 5 we provide extensive numerical examples to demonstrate the performance of the present marker and limiter with the SD method. Finally, conclusions and some possibilities for future work are given in Section 6.

2   Review of the spectral difference method

Consider the following hyperbolic conservation law

$$\frac{\partial Q}{\partial t} + \nabla \cdot \vec{F} = 0, \tag{2.1}$$

on domain $\Omega \times [0, T]$ and $\Omega \subset \mathbb{R}^d$ (d=2 or 3) with proper initial conditions within Ω and boundary conditions on $\partial \Omega$. The state variable Q can be a scalar or a vector, and the generalized flux $\vec{F}$ can be a scalar, vector, or tensor. In the case of the Euler equations, Q is the vector of conservative variables. Domain Ω is partitioned into non-overlapping triangular or quadrilateral cells (or elements). In the SD method, two sets of points, i.e., the solution points and flux points are defined in each element. The solution points are the locations where the nodal values of the state variable Q are specified. Flux points are the locations where the nodal values of fluxes are computed. The DOFs in the SD method are the conservative variables at the solution points. Fig. 1 displays the placement of solution and flux points for the third-order SD schemes on triangular and quadrilateral cells.
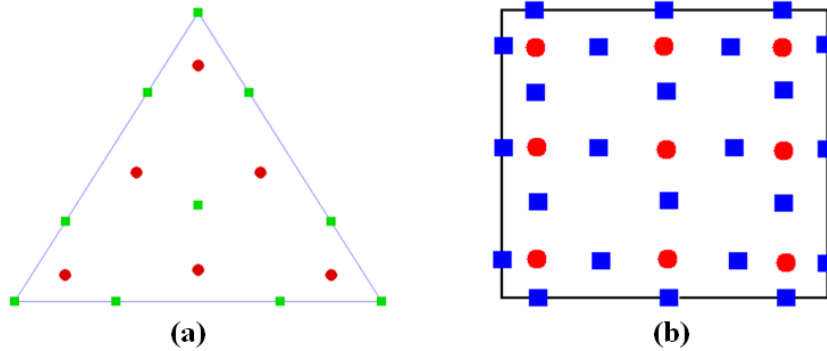
Figure 1: Solution (red solid circles) and flux points (green/blue solid squares). (a) Triangular mesh; (b) Quadrilateral mesh.

Given the solution $Q_{j,i}$ at the j-th solution point within cell i (denoted as $\vec{r}_{j,i}$), an element-wise degree p polynomial can be constructed using Lagrange-type polynomial base, i.e.,

$$p_i(\vec{r}) = \sum_{j=1}^{m} L_{j,i}(\vec{r}) Q_{j,i}, \tag{2.2}$$

where $L_{j,i}(\vec{r})$ are the Lagrange shape functions. With (2.2), the solutions at the flux points can be computed. Since the solutions are discontinuous across element boundaries, the fluxes at the element interfaces are not uniquely defined. Obviously, in order to ensure conservation, the normal component of the flux vector on each face should be identical for the two cells sharing the face. A one dimensional approximate Riemann solver [21, 31] is then employed in the face normal direction to compute the common normal flux $\hat{F}(Q^-, Q^+, \vec{n})$. Since the tangential component of the flux does not affect the conservation property, several choices are possible at the face flux points. Let the unit vector in the tangential direction be $\vec{l}$ as shown in Fig. 2. Here we offer two possibilities. One is to use a unique tangential component by averaging the two
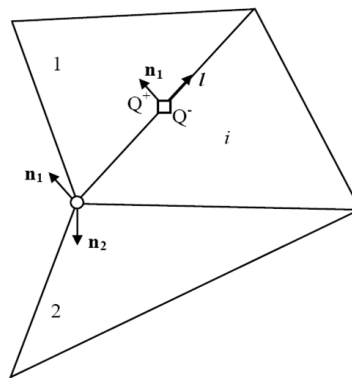

Figure 2: Flux computation.

tangential components from both sides of the face, i.e.,

$$F_l = F_l(Q^-, Q^+, \vec{l}) = \frac{1}{2}\{[\vec{F}(Q^-) + \vec{F}(Q^+)] \cdot \vec{l}\}. \tag{2.3}$$

The other option is to use their own tangential components separately, allowing discontinuous tangential components on the element interfaces. For cell i, the tangential component is $\vec{F}(Q^-) \cdot \vec{l}$, and for its neighbor $\vec{F}(Q^+) \cdot \vec{l}$. For a corner flux point in cell i, two faces (viewed from cell i) share the corner point, as shown in Fig. 2. The full flux vector at the corner point can be uniquely determined from the two normal Riemann flux components $\hat{F}_1 = \vec{F} \cdot \vec{n}_1$ and $\hat{F}_2 = \vec{F} \cdot \vec{n}_2$. In spite that the fluxes at a cell corner point do not have the same value for all the cells sharing the corner, local conservation is guaranteed because neighboring cells do share a common normal flux at all flux points. Once the fluxes at all flux points are re-computed, they are used to form a $p + 1$ degree polynomial, i.e.,

$$\vec{P}_i(\vec{r}) = \sum_{l=1}^{m_{p+1}} Z_{l,i}(\vec{r})\vec{F}_{l,i}, \tag{2.4}$$

where $\vec{F}_{l,i} = \vec{F}(\vec{r}_{l,i})$ and $Z_{l,i}(\vec{r})$ are the set of Lagrange shape functions defined by the flux points. The divergence of the flux at the solution points can be easily computed as,

$$\nabla \cdot \vec{P}_i(\vec{r}) = \sum_{l=1}^{m_{p+1}} \nabla Z_{l,i}(\vec{r}_{j,i}) \cdot \vec{F}_{l,i}. \tag{2.5}$$

Finally the semi-discrete scheme to update the solution unknowns can be written as

$$\frac{dQ_{j,i}}{dt} + \sum_{l=1}^{m_{p+1}} \nabla Z_{l,i}(\vec{r}_{j,i}) \cdot \vec{F}_{l,i} = 0. \tag{2.6}$$

The SD method for quadrilateral or hexahedral grid is identical to the staggered grid multi-domain spectral method [16,17]. It is particularly attractive because all the spatial operators are one-dimensional in nature. In the original staggered-grid method [16,17], the solution and flux points are the Chebyshev-Gauss and Chebyshev-Gauss-Lobatto points. Recently, it was found [12,37] that these flux points result in a weak instability for high-order schemes. New stable fluxes points were suggested in [12,37]. In the present study, we employ the Legendre-Gauss points plus the two end points as the flux points, as suggested in [12]. In an actual implementation, each physical element (possibly curved) is first transformed into a standard element (square). The governing equations are also transformed from the physical space to the computational space as follows

$$\frac{\partial \tilde{Q}}{dt} + \frac{\partial \tilde{F}}{\partial \xi} + \frac{\partial \tilde{G}}{\partial \eta} = 0, \tag{2.7}$$

where

$$\begin{bmatrix} \tilde{F} \\ \tilde{G} \end{bmatrix} = |J| \begin{bmatrix} \xi_x & \xi_y \\ \eta_x & \eta_y \end{bmatrix} \cdot \begin{bmatrix} F_x \\ F_y \end{bmatrix}, \qquad \tilde{Q} = |J| \cdot Q.$$

The Lagrange interpolation shape functions in one direction for the conservative solution variable Q and fluxes can be written as follows, respectively,

$$h_i(X) = \prod_{s=1,s\neq i}^{N} \left(\frac{X - X_s}{X_i - X_s} \right), \quad l_{i+1/2}(X) = \prod_{s=0,s\neq i}^{N} \left(\frac{X - X_{s+1/2}}{X_{i+1/2} - X_{s+1/2}} \right). \tag{2.8}$$

The reconstructed solution for the conservative variables in the standard element is just the tensor products of the three one-dimensional polynomials, i.e.,

$$\tilde{Q}(\xi,\eta) = \sum_{j=1}^{N} \sum_{i=1}^{N} \tilde{Q}_{i,j} h_i(\xi) h_j(\eta). \tag{2.9}$$

Similarly, the reconstructed flux polynomials take the following form:

$$\tilde{F}(\xi,\eta) = \sum_{j=1}^{N} \sum_{i=0}^{N} \tilde{F}_{i+1/2,j} l_{i+1/2}(\xi) h_j(\eta), \tag{2.10}$$

$$\tilde{G}(\xi,\eta) = \sum_{j=0}^{N} \sum_{i=1}^{N} \tilde{G}_{i,j+1/2} h_i(\xi) l_{j+1/2}(\eta). \tag{2.11}$$

For the inviscid flux, a Riemann solver is employed to compute a common flux at the interfaces to ensure conservation and stability. Time integration is done by using either explicit TVD or SSP Runge-Kutta scheme [32,33] or an implicit LU-SGS scheme [35,45].

3   Comparison of troubled cells markers

In this section, we first review and evaluate several troubled-cell detection methods found in the literature [27]. Then we present a parameter-free TVD marker.

Qiu and Shu [27] investigated seven markers currently used in the CFD community, and found that the minomd TVB marker [5], the marker developed by Krivodonova et al. named KXRCF in [19], and the Harten [11] marker are the best three among the seven markers they studied based on the amount of spurious oscillations in the solution, and the total number of cells marked. These three markers are chosen in the current study, and are evaluated next.

Consider the following 1D scalar conservation law

$$u_t + f(u)_x = 0, \quad x \in \Omega, \quad t > 0, \tag{3.1a}$$

$$u(x,0) = u_0(x), \quad x \in \Omega. \tag{3.1b}$$

The computational domain Ω is partitioned into N cells with $p + 1$ solution points and $p + 2$ flux points in each cell. In the following description, h_i, $\bar{u}_i$ and $u_{j,i}$ denote the mesh size of cell i, the average solution and the value of the reconstructed solution polynomial at the j-th flux point of the i-th cell, respectively.

3.1 Minmod TVB marker

A user specified parameter M is chosen, which is of the order of the solution's second derivative in a smooth region. Then the differences between the solutions at the cell interfaces and the cell-averaged solution are examined. Denote these differences $\triangle u_{i,L} = \bar{u}_i - u_{1,i}$ and $\triangle u_{i,R} = u_{p+2,i} - \bar{u}_i$. If the following inequalities are satisfied

$$|\triangle u_{i,L}| \leq Mh_i^2 \quad \text{and} \quad |\triangle u_{i,R}| \leq Mh_i^2, \tag{3.2}$$

the solution in cell i is considered smooth, and thus the cell is NOT a troubled cell. Otherwise, compute the following quantities

$$\triangle \tilde{u}_{i,L} = \min \text{mod} \left(\triangle u_{i,L}, \bar{u}_i - \bar{u}_{i-1}, \bar{u}_{i+1} - \bar{u}_i \right), \tag{3.3}$$

$$\triangle \tilde{u}_{i,R} = \min \text{mod} \left(\triangle u_{i,R}, \bar{u}_i - \bar{u}_{i-1}, \bar{u}_{i+1} - \bar{u}_i \right), \tag{3.4}$$

where the minmod function is defined as

$$\min \text{mod} \left(a_1, a_2, \cdots, a_n \right) = \begin{cases} s \cdot \min_{1 \leq k \leq n} |a_k|, & \text{if } sign(a_1) = \cdots = sign(a_n) = s, \\ 0, & \text{otherwise.} \end{cases} \tag{3.5}$$

If either $\triangle u_{i,L}$ or $\triangle u_{i,R}$ are modified in (3.3) or (3.4), i.e., $\triangle \tilde{u}_{i,L} \neq \triangle u_{i,L}$ or $\triangle \tilde{u}_{i,R} \neq \triangle u_{i,R}$, the cell is marked a troubled cell. Eqs. (3.3) and (3.4) are similar to the MUSCL scheme [39] in spirit, but not as restrictive. In order to explain this, assume the solution to be linear with a slope of S_i in cell i. Then we have

$$\triangle u_{i,L} = \triangle u_{i,R} = S_i h_i / 2. \tag{3.6}$$

Define two more slopes using

$$S_{i+1/2} = \frac{\bar{u}_{i+1} - \bar{u}_i}{x_{i+1} - x_i}, \quad S_{i-1/2} = \frac{\bar{u}_i - \bar{u}_{i-1}}{x_i - x_{i-1}}. \tag{3.7}$$

The following equation is equivalent to (3.3) and (3.4),

$$\tilde{S}_i = \min \text{mod} \left(S_i, S_{i-1/2} \frac{h_{i-1} + h_i}{h_i}, S_{i+1/2} \frac{h_i + h_{i+1}}{h_i} \right), \tag{3.8}$$

where $\tilde{S}_i$ is the limited slope. We have used $x_{i+1} - x_i = (h_{i+1} + h_i)/2$ and $x_i - x_{i-1} = (h_{i-1} + h_i)/2$ in (3.8). If the mesh is uniform, then the factors $(h_{i-1} + h_i)/h_i$ and $(h_{i+1} + h_i)/h_i$ become 2. If the mesh is extremely non-uniform, the factors can approach 1. In practice, we could use a factor between 1 and 2, i.e.,

$$\tilde{S}_i = \min \text{mod} \left(S_i, \beta \frac{\bar{u}_i - \bar{u}_{i-1}}{x_i - x_{i-1}}, \beta \frac{\bar{u}_{i+1} - \bar{u}_i}{x_{i+1} - x_i} \right). \tag{3.9}$$

The larger β is, the fewer number of cells is marked at the expense of possibly missing some troubled cells. A good compromise is $\beta = 1.5$. Obviously if the solution is locally linear, the cell is not marked because

$$S_i = \frac{\bar{u}_i - \bar{u}_{i-1}}{x_i - x_{i-1}} = \frac{\bar{u}_{i+1} - \bar{u}_i}{x_{i+1} - x_i}.$$

Eq. (3.9) will be used again to design marker and limiters.

As pointed out in [27], $M > 0$ is a free parameter, which depends on the solution of the problem. For scalar problems it is possible to estimate M if the solution is smooth [5] (M is proportional to the second derivative of the initial condition at smooth extrema). However it is more difficult to estimate M for the systems case, such as the Euler and N-S equations. If M is chosen too small, more cells than necessary will be marked as troubled cells. If M is chosen too large, spurious oscillations may appear.

3.2   KXRCF marker

In [19] Krivodonova et al. proposed a shock-detection technique based on DG's super-convergence property at the outflow boundaries of an element in smooth regions. This method was termed the KXRCF marker. The boundary of a cell, ∂I_i, can be partitioned into two portions: the inflow boundary ∂I_i^- where flow goes into the cell, and the outflow boundary ∂I_i^+ where flow exits the cell. In the 1D case, if the wave speed $f'(u)$ is positive at the left interface, then the left face ($x_{i-1/2}$) is an inflow boundary; otherwise, the left face is an outflow boundary. The right face can be classified in exactly the opposite fashion. In an actual implementation, we use the averaged wave speed from both sides of a face to determine if it is an inflow or outflow boundary. The KXRCF marker checks the solution on the inflow boundary to determine troubled cells. Without loss of generality, let's assume the inflow boundary is the left interface for cell i. Then compute the following quantity L_i,

$$L_i = \frac{|u_{1,i} - u_{p+2,i-1}|}{h_i^{(p+1)/2}|\bar{u}_i|}. \tag{3.10}$$

If $L_i > 1$, then cell i is marked as a troubled cell. Note that since DG's super-convergence property occurs only in a smooth region, the KXRCF marker might unnecessarily mark some cells in continuous but not smooth regions.

3.3   Harten/ modified Harten marker

The Harten marker was originally developed in [11] and further modified in [27]. Here is the basic idea. First extend the reconstructed solution polynomials from the neighboring cells $u_{i-1}(x)$ and $u_{i+1}(x)$ into cell i. Then compute the differences between the average extended polynomials and the average of cell i. In 1D, a jump (discontinuity) within cell i can cause one extension above the current cell average and the other below the current cell average. Therefore the Harten marker can be formulated as follows. Compute

$$F_i(z) = \frac{1}{h_i}\left\{ \int_{x_{i-1/2}}^{z} u_{i-1}(x)dx + \int_{z}^{x_{i+1/2}} u_{i+1}(x)dx \right\} - \bar{u}_i. \tag{3.11}$$

If

$$F_i(x_{i+1/2}) \cdot F_i(x_{i-1/2}) \leq 0, \tag{3.12}$$

then a discontinuity possibly exists within cell i. To improve its performance at smooth extrema, the cell-averaged degree p derivatives between the neighboring cells and the current cell are also compared. Thus, if

$$F_i(x_{i+1/2}) \cdot F_i(x_{i-1/2}) \leq 0, \quad |\bar{u}_i^{(p)}| > \theta|\bar{u}_{i-1}^{(p)}| \quad \text{and} \quad |\bar{u}_i^{(p)}| > \theta|\bar{u}_{i+1}^{(p)}|, \tag{3.13}$$

cell i is marked as a troubled cell. We take the same value for the constant $\theta(=1.5)$ in the numerical tests as in [27].

We can make the following observations regarding the Harten marker. When the polynomial degree p is high, the extension of the reconstructed solution polynomials from the neighboring cells might be strange and unexpected near a discontinuity, and may fail to mark a shock, as shown in Fig. 7. In this case, the extended polynomials from both sides have cell averaged solutions larger than the current cell. Therefore this strategy may fail to mark a discontinuity in a high-order scheme. The Harten marker is difficult to implement for unstructured grids in multiple dimensions.

To illustrate the performance of the above three markers, examples of both smooth and discontinuous solution profiles have been used:

i) A smooth sine function, $u=\sin(2\pi x)$, $0 \leq x \leq 1$;

ii) A combination of smooth and discontinuous profiles: a smooth Gaussian, a square pulse, a triangle and half an ellipse [18], which is defined as

$$u_0(x) = \begin{cases} (G(x,\beta,z-\delta)+G(x,\beta,z+\delta)+4G(x,\beta,z))/6, & -0.8 \leq x \leq -0.6, \\ 1, & -0.4 \leq x \leq -0.2, \\ 1-|10(x-0.1)|, & 0 \leq x \leq 0.2, \\ (F(x,\alpha,a-\delta)+F(x,\alpha,a+\delta)+4G(x,\alpha,z))/6, & 0.4 \leq x \leq 0.6, \\ 0, & \text{otherwise}, \end{cases} \tag{3.14}$$

$$G(x,\beta,z) = e^{-\beta(x-z)^2}, \qquad F(x,\alpha,a) = \sqrt{\max(1-\alpha^2(x-a)^2,0)}, \tag{3.15}$$

where $a=0.5$, $z=-0.7$, $\delta=0.005$, $\alpha=10$, $\beta=\log 2/(36\delta^2)$.

iii) An oscillatory shock profile obtained when solving nonlinear hyperbolic equations.

The marked cells for the initial profiles are then plotted. In the following figures, the solid black lines stand for the initial profile, and the elevated red squares represent the troubled cell.

The Minmod TVB marker works well for the scalar cases as shown in Fig. 3(a) and 3(b), where no cell is marked as troubled cell for the smooth sine wave, and only the cells at the discontinuity region are marked as troubled cells. Here we estimated M from [5] by computing the maximum absolute value of the second derivatives of the initial solution in smooth regions for each of the two cases. However, for the complex oscillatory shock profile case in Fig. 4, it is difficult to estimate M from this initial profile. It appears that $M=40$ works well in that only the two cells at the discontinuity
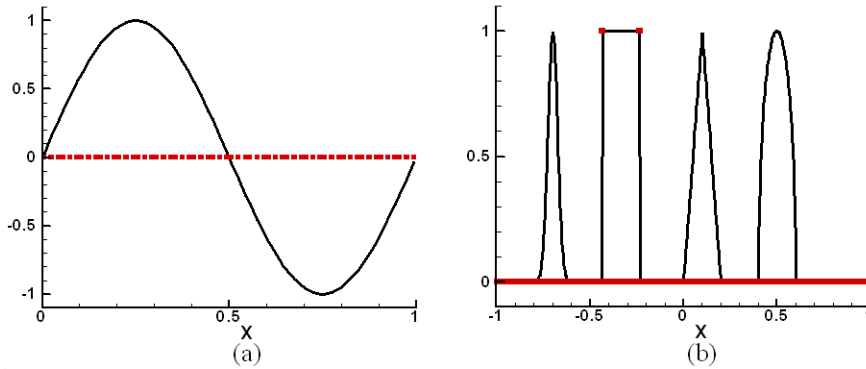
Figure 3: Minmod TVB marker by using M from [5] (p=2). (a) sine wave, 20 cells; (b) discontinuous profile [18], 200 cells, p=2.
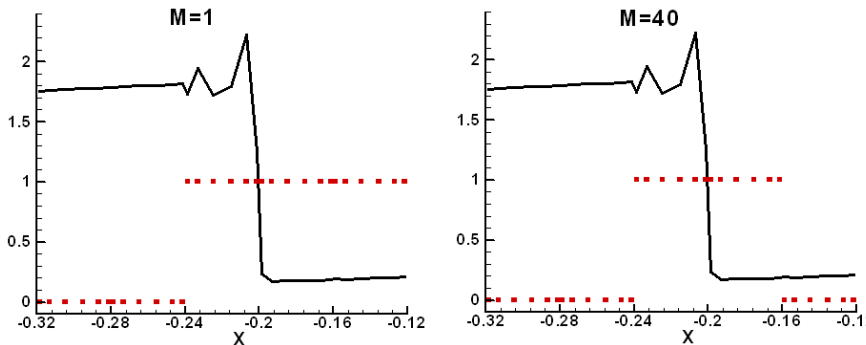

Figure 4: Minmod TVB marker for the oscillating shock profile with different M (5 cells), p=6.

are marked as troubled cells. But we found M=40 by ad hoc testing. For the system cases such as Euler and Navier-Stokes equations, it is more difficult to estimate M.

The KXRCF marker detects the discontinuities as shown in Fig. 5(b) and Fig. 6. It also works well for the smooth sine wave case in Fig. 5(a) as well as the smooth Gaussian extremum in Fig. 5(b) (see the close-up view in Fig. 5(c)), where no troubled cell at the local smooth extrema is marked. This is expected because the KXRCF marker is exactly based on the super-convergence property on the elements' outflow boundaries in smooth regions. However, in continuous but not smooth regions, such as the vicinity of x=-0.8 in Fig. 5(b) or x=-0.16 in Fig. 6, the KXRCF marker can unnecessarily mark the cells in those continuous regions as troubled cells.

The Modified Harten marker gives good results in the smooth sine wave case, as shown in Fig. 8. The results for the discontinuous profile case are acceptable, but its performance is sensitive to the interpolation order of polynomial as shown in Fig. 9, where some more cells are marked when p=5 than the p=2 case. This sensitivity can cause a serious problem in the high-order cases as shown in Fig. 7, where the necessary condition (3.12) of the Harten marker fails to mark the shock cell. This is because that the extensions of the solution polynomials from the neighboring cells can
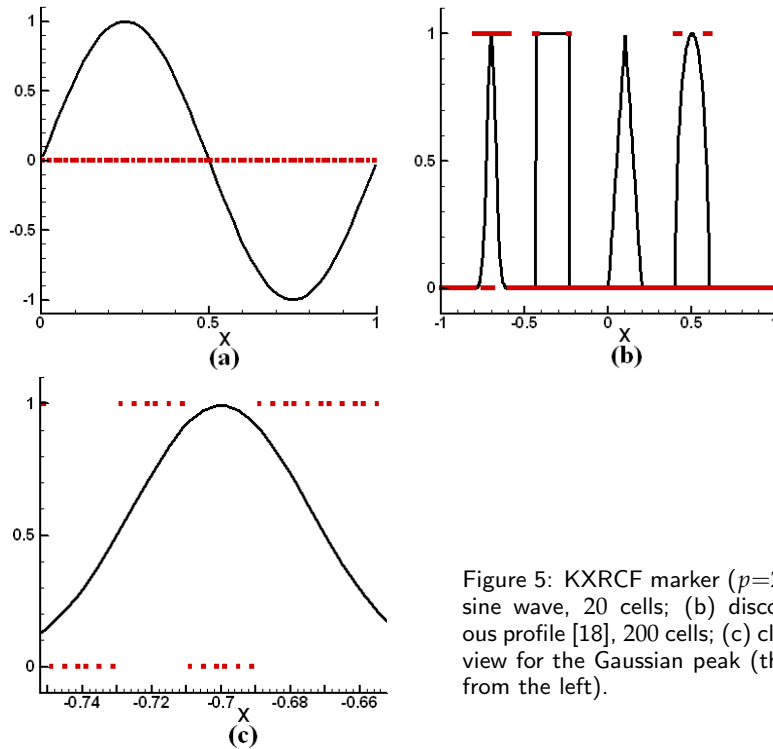
Figure 5: KXRCF marker ($p=2$). (a) sine wave, 20 cells; (b) discontinuous profile [18], 200 cells; (c) close-up view for the Gaussian peak (the first from the left).

become large in the current cell, and the integral values from the left and the right cells are all positive, i.e.,

$$F_i(x_{i-1/2}) = 1.886, \qquad F_i(x_{i+1/2}) = 7.22.$$

That is why the Modified Harten marker fails in this typical case.

3.4 Accuracy-Preserving TVD (AP-TVD) marker

The above examples show that the free parameters in the minmod TVB marker can have decisive effects on the performance of the marker; the KXRCF marker can mark
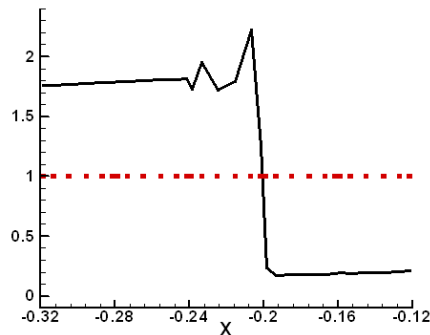
Figure 6: KXRCF marker for an oscillating shock profile (5 cells, $p=6$).
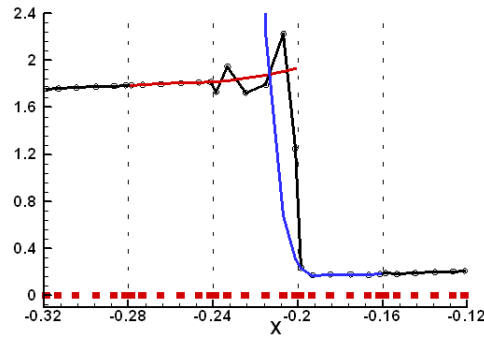
Figure 7: Harten condition (3.12) (5 cells, $p=6$) cells. Circle: solution points; Blue line: extension from right; Red line: extension from the left.
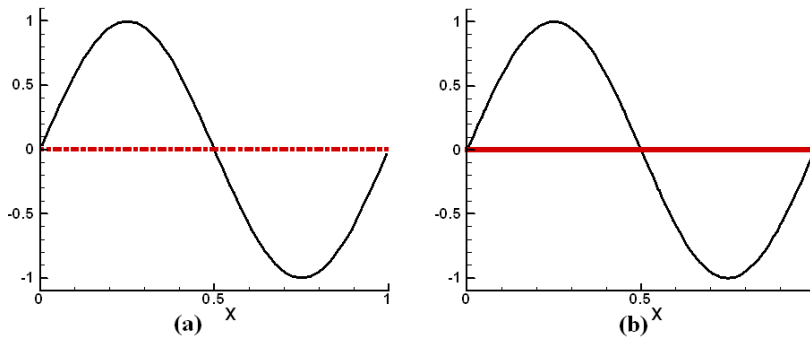

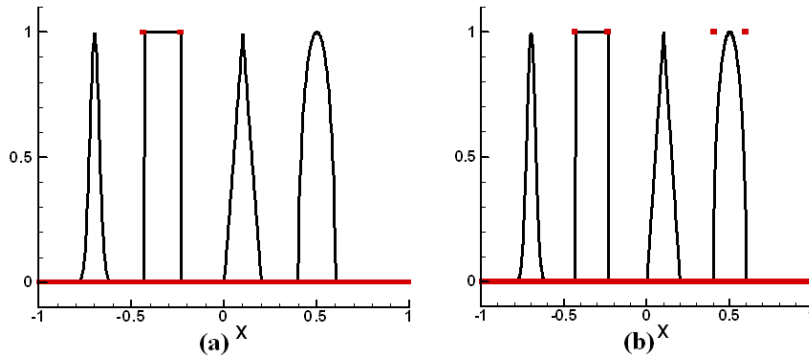Figure 8: Modified Harten marker for a sine wave with 20 cells. (a) $p=2$; (b) $p=5$.

Figure 9: Modified Harten marker for the discontinuous profile with 200 cells. (a) $p=2$; (b) $p=5$.

too many cells in continuous regions as troubled cells; the Harten marker can fail to detect a shock at a high-order setting, due to the unexpected polynomial extensions from the neighboring cells. In addition, the Harten marker is difficult to implement in 2D and 3D. Although it is impossible to design a perfect marker, one design goal we hope to achieve is a marker free of user-specified parameters.

In the minmod TVB marker, if parameter M is 0, it becomes a TVD marker. A well known drawback of the TVD marker is that cells at smooth solution extrema are marked. In order to unmark these smooth extrema, the first derivatives of the

solutions are examined to see if they are locally monotonic. This marker is divided into the following steps.

---

1. Compute the cell averaged solutions at each cell. Then compute the min and max cell averages for cell i from a local stencil using

$$\bar{u}_{max,i} = \max(\bar{u}_{i-1}, \bar{u}_i, \bar{u}_{i+1}) \quad \text{and} \quad \bar{u}_{min,i} = \min(\bar{u}_{i-1}, \bar{u}_i, \bar{u}_{i+1}). \quad (3.16)$$

If $\quad u_{j,i} > \bar{u}_{max,i} + 0.001|\bar{u}_{max,i}| \quad$ or $\quad u_{j,i} < \bar{u}_{min,i} - 0.001|\bar{u}_{min,i}|, \quad (j = 1, \ p+2), \quad (3.17)$

the cell i is considered as a possible troubled cell, which is further examined in the next step.

2. This step is aimed to unmark those cells at local extrema that are unnecessarily marked as troubled cells in the first step (3.17). If an extremum is smooth, the first derivative of the solution should be locally monotonic. Therefore, a minmod TVD marker is applied to see if the second derivative is bounded by the slopes computed with the cell-averaged first-derivatives. Compute

$$\tilde{u}_i^{(2)} = \text{minmod} \ (\bar{u}_i^{(2)}, \beta \frac{\bar{u}_{i+1}^{(1)} - \bar{u}_i^{(1)}}{x_{i+1} - x_i}, \beta \frac{\bar{u}_i^{(1)} - \bar{u}_{i-1}^{(1)}}{x_i - x_{i-1}}). \quad (3.18)$$

If $\tilde{u}_i^{(2)} = \bar{u}_i^{(2)}$, the cell is unmarked, i.e., not a troubled cell anymore. Otherwise, the cell is confirmed as a troubled cell. Obviously, this marker works for $p > 1$.

The coefficient 0.001 in (3.17) is not problem-dependent free parameters. It is used to overcome machine error when comparing two real numbers so as to avoid the trivial case that the solution is constant in the neighborhood. In order to compare the performance of the new AP-TVD marker with the Minmod TVB marker, the KXRCF marker, and the Modified Harten marker, we use the same three testing cases as before. Fig. 10 shows that the present AP-TVD marker performs consistently well at the local extrema regions for all the polynomial order $p > 1$. No cell is marked as a troubled cell in this smooth case as expected. Fig. 11 shows that the present marker detects the discontinuities without unnecessarily marking other cells in smooth regions. It also shows the consistently good performance of detecting discontinuity for all the polynomial order $p > 1$. Fig. 12 shows the present marker only marks the two cells at the discontinuity as expected, none elsewhere, in contrast to the other markers.

Comparing with the three "preferred" markers from [27], the present accuracy preserving TVD marker has shown the advantages that (1) no free-parameter and problem-independent; (2) is efficient in terms of the number of marked cells over the total number of cells and it performs well in marking the discontinuities; (3) it is compact and easy to implement for arbitrary unstructured meshes.

4   Formulation of the generalized moment limiter

Next we present a p-exact high-order accuracy-preserving limiter based on the moment limiter [2, 23] and cell averages. The present limiter uses a Taylor-series-like
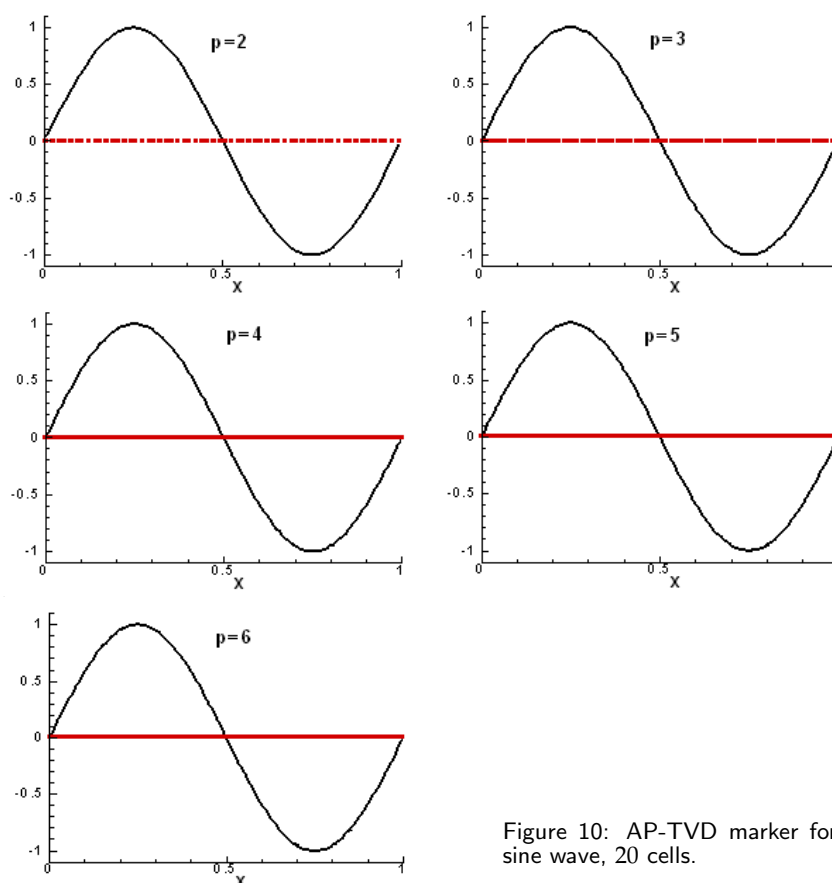
Figure 10: AP-TVD marker for the sine wave, 20 cells.

expansion for the reconstruction, which is similar to that in [23]. The difference is that the expansion is performed with respect to the cell-averaged derivatives, rather than the derivatives at a specific point such as the cell centroid. Then these cell-averaged derivatives are limited in a hierarchical manner starting from the highest derivative. Combined with the AP-TVD marker, this new limiting technique exhibits the following properties: (1) free of problem-dependent parameters; (2) unstructured-grid based, easy to implement for 3D arbitrary meshes, and compact for parallel computing; (3) capable of suppressing spurious oscillations near solution discontinuities without loss of accuracy at the local extrema in the smooth regions. We will call this limiting technique "parameter-free generalized moment limiter" (or termed as "PFGM limiter").

In the SD method the solution points are used to construct a degree p polynomial that can recover the conservative variables at the flux points. This reconstruction can produce spurious oscillations near a shock wave. Therefore a new non-oscillatory reconstruction is needed in the troubled cells. The following idea is followed. First the original degree p solution polynomial within a "troubled cell" is replaced with an equivalent polynomial based on the cell-averaged derivatives up to degree p. Then the
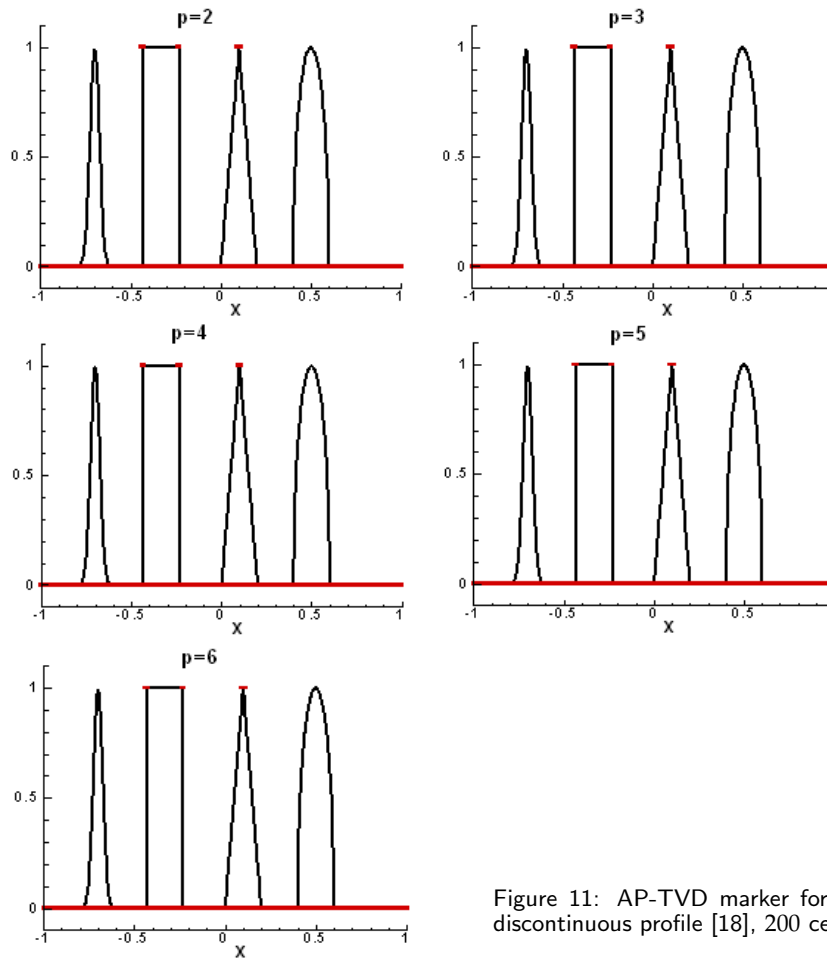
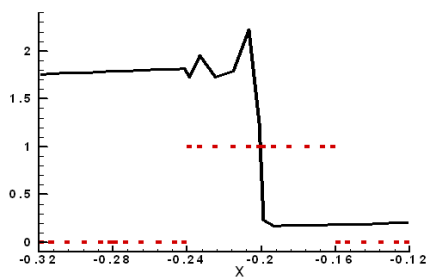Figure 11: AP-TVD marker for the discontinuous profile [18], 200 cells.

Figure 12: AP-TVD marker for the oscillating shock profile (5 cells, $p=6$).

high-order derivatives are hierarchically limited using the cell-averaged derivatives of one degree lower. In case that the highest derivative is not altered, the original polynomial is preserved. This procedure can be easily implemented for unstructured-grid based high-order methods.

Let's consider the 1D case first. Let the original solution polynomial before limiting be $u_i(x)$, and the limited polynomial be $Y_i(x)$ within cell i. First we express $u_i(x)$ in

terms of the cell-averaged derivatives up to degree p, i.e.,

$$u_i(x) = \bar{u}_i + \bar{u}_i^{(1)}(x - x_i) + \frac{1}{2}\bar{u}_i^{(2)}\left((x - x_i)^2 - \frac{1}{12}h_i^2\right) + \frac{1}{6}\bar{u}_i^{(3)}\left((x - x_i)^3 - \frac{1}{4}h_i^2(x - x_i)\right)$$

$$+ \frac{1}{24}\bar{u}_i^{(4)}\left((x - x_i)^4 - \frac{1}{2}h_i^2(x - x_i)^2 + \frac{7}{240}h_i^4\right) + \cdots \qquad (4.1)$$

where x_i represents the cell centroid coordinate.

Next the cell-averaged derivatives are limited in a hierarchical manner by using a minmod-type limiter. Starting from the highest-order derivative, $\bar{u}^{(p)}$ is limited using,

$$\bar{Y}_i^{(p)} = \min\text{mod}\left(\bar{u}_i^{(p)}, \beta\frac{\bar{u}_{i+1}^{(p-1)} - \bar{u}_i^{(p-1)}}{x_{i+1} - x_i}, \beta\frac{\bar{u}_i^{(p-1)} - \bar{u}_{i-1}^{(p-1)}}{x_i - x_{i-1}}.\right) \qquad (4.2)$$

If $\bar{Y}_i^{(p)} = \bar{u}_i^{(p)}$, the highest derivative is not altered. No further limiting is required, and solution remains the same. Otherwise, the limiting process proceeds to the next lower derivative in a similar fashion, i.e.,

$$\bar{Y}_i^{(k)} = \min\text{mod}\left(\bar{u}_i^{(k)}, \beta\frac{\bar{u}_{i+1}^{(k-1)} - \bar{u}_i^{(k-1)}}{x_{i+1} - x_i}, \beta\frac{\bar{u}_i^{(k-1)} - \bar{u}_{i-1}^{(k-1)}}{x_i - x_{i-1}}\right), \quad k = p - 1. \qquad (4.3)$$

If $\bar{Y}_i^{(p-1)} = \bar{u}_i^{(p-1)}$, none of the lower derivative are further limited, i.e.,

$$\bar{Y}_i^{(k)} = \bar{u}_i^{(k)}, \quad (k = p - 2, \cdots, 1). \qquad (4.4)$$

Otherwise, the process continues in a similar fashion hierarchically until the first derivative is limited. In order to preserve the mean, the zero-th derivative (the mean) is retained, i.e., $\bar{Y}_i = \bar{u}_i$. Finally the limited polynomial is written as

$$Y_i(x) = \bar{Y}_i + \bar{Y}_i(x - x_i) + \frac{1}{2}\bar{Y}_i^{(2)}\left((x - x_i)^2 - \frac{1}{12}h_i^2\right) + \frac{1}{6}\bar{Y}_i^{(3)}\left((x - x_i)^3 - \frac{1}{4}h_i^2(x - x_i)\right)$$

$$+ \frac{1}{24}\bar{Y}_i^{(4)}\left((x - x_i)^4 - \frac{1}{2}h_i^2(x - x_i)^2 + \frac{7}{240}h_i^4\right) + \cdots \qquad (4.5)$$

Note that this limiter is compact, only involving data from its immediate neighbors, and easy to implement. Next we present an efficient extension to multi-dimensional unstructured grids. Similar to the 1D case, we first express the solution polynomial with respect to the cell-averaged derivatives,

$$u_i(x, y) = \bar{u}_i + \bar{u}_{x,i}\triangle x + \bar{u}_{y,i}\triangle y + \frac{1}{2}\bar{u}_{xx,i}(\triangle x^2 - I_{xx})$$

$$+ \frac{1}{2}\bar{u}_{yy,i}(\triangle y^2 - I_{yy}) + \bar{u}_{xy,i}(\triangle x\triangle y - I_{xy}), \qquad (4.6)$$

where

$$\triangle x = x - x_i, \qquad \triangle y = y - y_i, \qquad \triangle x^2 = (x - x_i)^2,$$

$$\triangle y^2 = (y - y_i)^2, \qquad x_i \equiv \frac{1}{V_i}\int_{V_i} x dV, \qquad y_i \equiv \frac{1}{V_i}\int_{V_i} y dV,$$

$$I_{xx} \equiv \frac{1}{V_i}\int_{V_i} \triangle x^2 dV, \quad I_{yy} \equiv \frac{1}{V_i}\int_{V_i} \triangle y^2 dV, \quad I_{xy} \equiv \frac{1}{V_i}\int_{V_i} \triangle x\triangle y dV.$$

We proceed to limit the cell-averaged derivatives involved in (4.6) for the troubled cells. In multiple dimensions, especially in 3D, the efficiency of the limiter is a very important criterion. In order to achieve the highest efficiency, we decide to limit the derivatives of the same degree altogether with a scalar factor between 0 and 1, i.e., the limited polynomial can be written as

$$Y_i(x,y) = \bar{u}_i + \alpha^{(1)}(\bar{u}_{x,i}\triangle x + \bar{u}_{y,i}\triangle y) + \alpha^{(2)}\Big\{\frac{1}{2}\bar{u}_{xx,i}(\triangle x^2 - I_{xx})$$

$$+\frac{1}{2}\bar{u}_{yy,i}(\triangle y^2 - I_{yy}) + \bar{u}_{xy,i}(\triangle x\triangle y - I_{xy})\Big\}, \tag{4.7}$$

where $\alpha^{(1)}$ and $\alpha^{(2)}$ are the scalar limiters for the first and second derivatives in $[0,1]$. The essential 1D idea is then generalized into 2D and 3D. The limiter is conducted in the following steps assuming $p=2$:

1. Compute the cell averaged 2nd order derivatives in the troubled cell, and the cell-averaged 1st order derivatives in the troubled cell and its immediate face neighbors, as shown in Fig. 13. Since the 2nd order derivatives are constants, and the 1st order derivatives are linear, we can assume that the cell-averaged 1st order derivatives are the first order derivatives at the cell centroids, i.e., $\bar{u}_{x,i}=u_{x,i}(x_i,y_i)$ and $\bar{u}_{y,i}=u_{y,i}(x_i,y_i)$.

2. Assume one of the face neighbors is cell j. Define the unit vector connecting the centroids of cell i and cell j as $\vec{l}$. The 2nd order derivative in this direction is examined next to determine whether limiting is necessary. Compute this second-order derivative according to

$$u_{ll,i} = \bar{u}_{xx,i}l_x^2 + \bar{u}_{yy,i}l_y^2 + 2\bar{u}_{xy,i}l_xl_y.$$

3. Compute the first derivative in $\vec{l}$ at the centroids of for both cell i and j,

$$u_{l,i}(x_i,y_i) = \bar{u}_{x,i}l_x + \bar{u}_{y,i}l_y, \quad u_{l,j}(x_j,y_j) = \bar{u}_{x,j}l_x + \bar{u}_{y,j}l_y.$$

Estimate the 2nd-derivative using

$$u_{\tilde{ll},i} = \frac{u_{l,j}(x_j,y_j) - u_{l,i}(x_i,y_i)}{|\vec{r}_i - \vec{r}_j|}.$$

4. Finally the scalar limiter for this face is computed according to

$$\alpha_{ij}^{(2)} = \text{minmod}(1, \beta\tilde{u}_{ll,i}/u_{ll,i}). \tag{4.8}$$

The process is repeated for the other faces. Finally, the scalar limiter for the cell is the minimum of those computed for the faces, i.e.,

$$\alpha^{(2)} = \min_j(\alpha_{ij}^{(2)}). \tag{4.9}$$

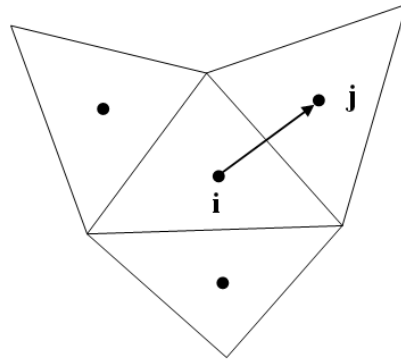If $\alpha^{(2)}=1$, the 2nd order derivatives are not altered. The solution polynomial remains

Figure 13: Schematic of multidimensional limiting.

the same. Otherwise, the 1st order derivatives are limited in a similar fashion to compute $\alpha^{(1)}$, i.e.,

$$\alpha_{ij}^{(1)} = \min \mathrm{mod} \left(1, \beta \tilde{u}_{l,i}/u_{l,i} \right), \tag{4.10}$$

where $\tilde{u}_{l,i} \equiv (\bar{u}_j - \bar{u}_i)/|\vec{r}_i - \vec{r}_j|$. Finally,

$$\alpha^{(1)} = \min_j (\alpha_{ij}^{(1)}). \tag{4.11}$$

As can be seen, this generalized moment limiter keeps its compactness for arbitrary unstructured meshes, and can preserve a locally degree p polynomial, therefore satisfying the p-exact property.

5 Numerical tests

In this section we provide extensive numerical experimental results to demonstrate the performance of the PFGM limiter described in Section 4. In the numerical tests, the three-stage explicit TVD Runge-Kutta scheme [22] was used for time integration, unless otherwise noted.

5.1 Accuracy study with smooth problems

5.1.1 Linear scalar wave equation

Consider the 1D linear wave equation

$$u_t + u_x = 0, \tag{5.1}$$

with initial condition $u(x,0) = \sin(2\pi x)$, and periodic boundary conditions. The CFL number (CFL=$f'(u)\triangle x = \triangle t/\triangle x$) used for each case is as follows: (1) if p=1, 2, 3, CFL=0.01; (2) if p=4, 5, CFL=0.001. These CFL numbers are small enough so that the error is dominated by the spatial discretization. In this test, we did not use the AP-TVD marker so that the generalized moment limiter is applied to every cell in order
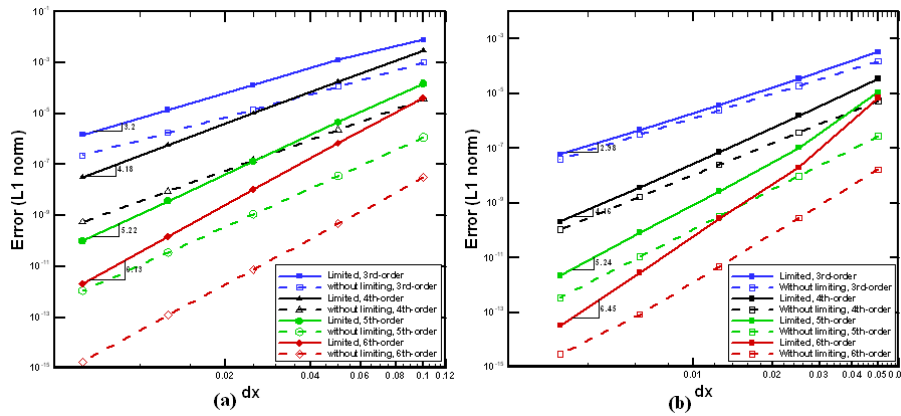
Figure 14: Grid convergence of the present limiter. (a) Linear advection equation (5.1) for sine wave at $t=1$; (b) Non-linear Burgers equation (5.2) at $t=0.1$.

to test the performance of the limiter alone. Otherwise, none of the cells would be marked and the results would be the same as the unlimited schemes. The L_1 error at $t=1$ for various schemes with and without the limiter are shown in Fig. 14(a). We can see that the present limiter preserves the designed order of accuracy of the original SD method, although the magnitude of the error is larger than the unlimited schemes.

5.1.2 Nonlinear Burgers equation

Next consider the 1D non-linear Burgers equation

$$u_t + \frac{1}{2}(u^2)_x = 0, \tag{5.2}$$

with initial condition $u(x,0)=1+\sin(\pi x)$, periodic boundary conditions. The CFL number used for each case is as follows: (1) if $p=1$, 2, 3, CFL=0.01; (2) if $p=4$, 5, CFL=0.001. The solution errors at $t=0.1$ (when the solution is still smooth) are shown in Fig. 14(b). Again we can see that the present limiter preserves the designed order of accuracy of the original SD method. The results are quite similar to the linear scalar wave case.

5.2 1D problems with discontinuities

5.2.1 Combined smooth and discontinuous waves

We solve the 1D wave equation (5.1) at $t=8$ with the initial condition [18] as plotted in Fig. 15. Periodic boundary conditions were used. A uniform mesh is used with a total of 200 cells. The CFL number used for each case is as follows: (1) if $p=1$, 2, CFL=0.01; (2) if $p=3$, 4, 5, CFL=0.001. The long time evolution ($t=8$) was considered in order to check the performance of the high-order schemes. The numerical solution is plotted at each solution point (red square). As seen that the present PFGM limiter yields good results at both the smooth region (as for the local extrema of the first jump) and discontinuities.
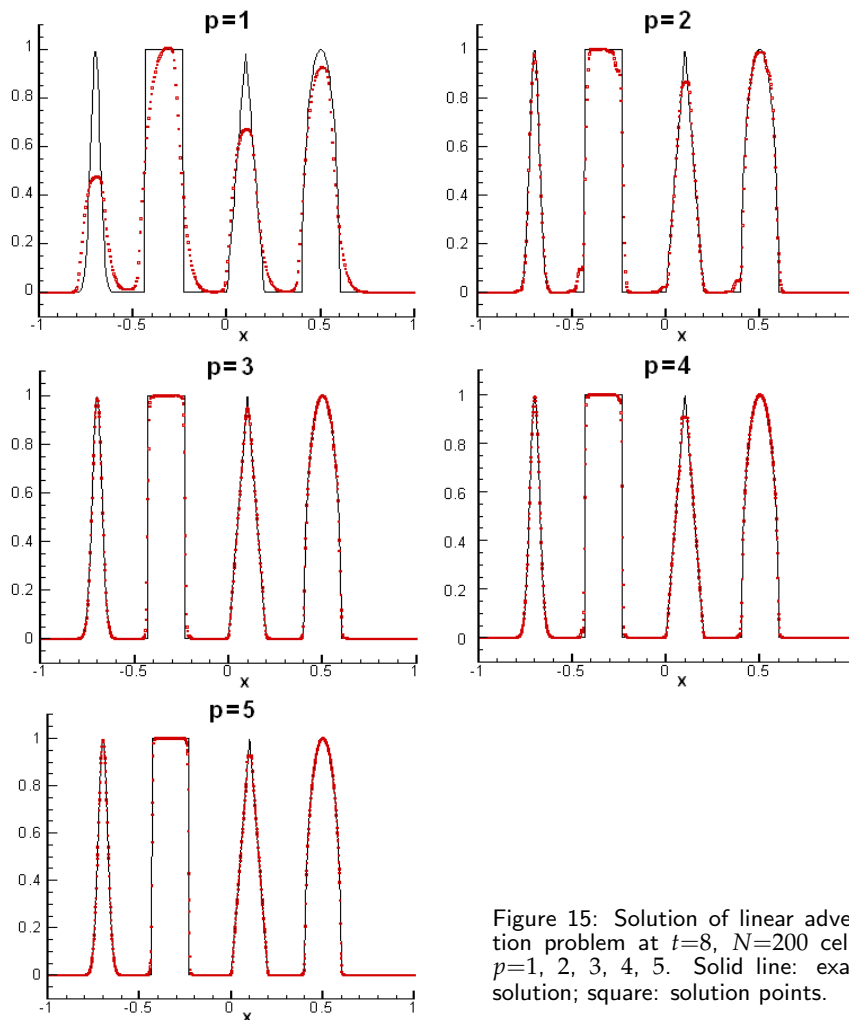
Figure 15: Solution of linear advection problem at $t=8$, $N=200$ cells, $p=1$, 2, 3, 4, 5. Solid line: exact solution; square: solution points.

5.2.2 Burgers equation with shock

In this example the Burgers equation (5.2) was solved with the same initial conditions and periodic boundary conditions as in 5.2.2, but until $t=0.8$ when a shock appears. The CFL number used for each case is as follows: (1) if $p=1$, 2, CFL=0.01; (2) if $p=3$, 4, 5, CFL=0.001. A mesh with 100 uniform cells was used with various schemes. The shock was captured well without oscillations, as shown in Fig. 16.

5.2.3 Sod shock-tube problem

Sod shock-tube problem was solved to test the limiter for the Euler equations

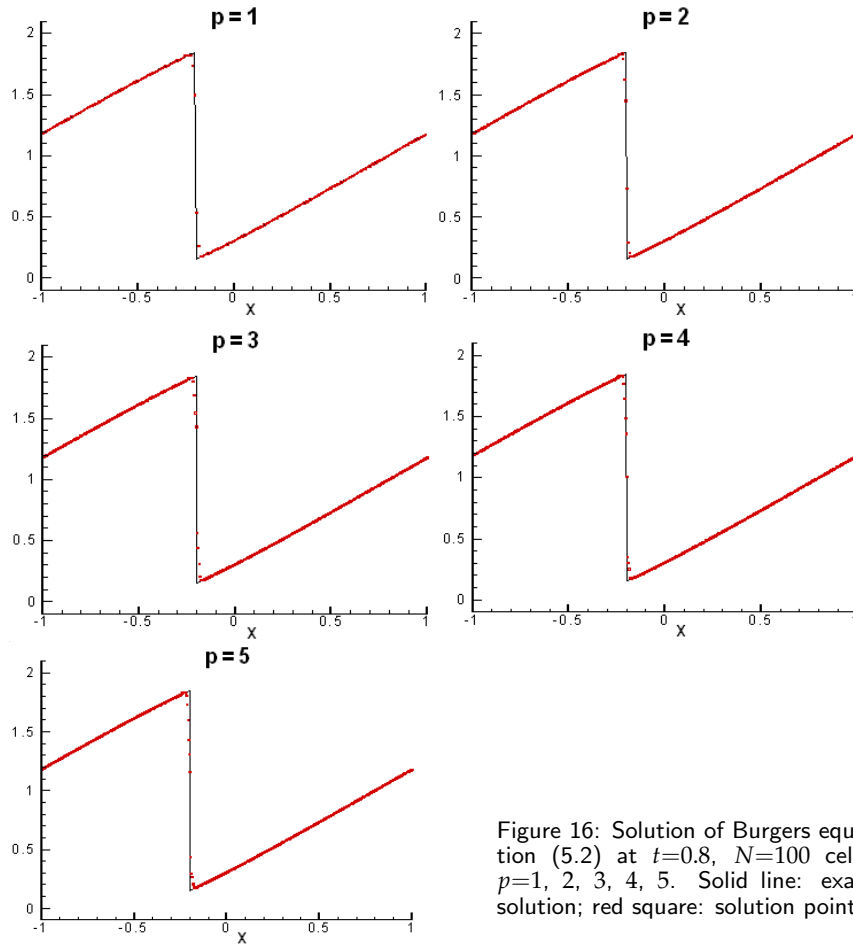$$u_t + f(u)_x = 0, \tag{5.3}$$

Figure 16: Solution of Burgers equation (5.2) at t=0.8, N=100 cells, p=1, 2, 3, 4, 5. Solid line: exact solution; red square: solution points.

where

$$u = (\rho, \rho v, E)^{\mathrm{T}}, \qquad f(u) = (\rho v, \rho v^2 + p, v(E + p))^{\mathrm{T}},$$

$$E = \frac{p}{\gamma - 1} + \frac{1}{2}\rho v^2, \qquad \gamma = 1.4,$$

and ρ, v, E, p are the density, velocity, total energy, and pressure, respectively. The initial condition is

$$(\rho, p, v) = \begin{cases} (1, 1, 0) & \text{for } x < 0, \\ (0.125, 0.1, 0) & \text{for } x \geq 0. \end{cases}$$

In Fig. 17, the computed density at t=2 with the present PFGM limiter is compared with the exact solution for p=1, 2, 3, 4. The time step size used for each case is as follows: (1) if p=1, 2, dt=0.001; (2) if p=3, 4, dt=0.0005. Note that the solutions appear oscillation-free, and both the shock and contact were well captured. The higher-order scheme appears to yield better results.
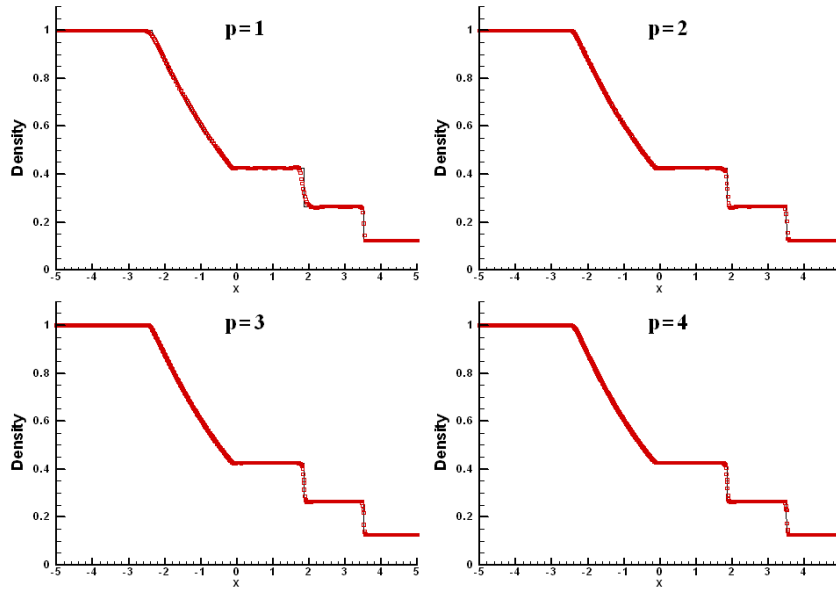
Figure 17: Sod problem, $t=2$, $N=200$ cells, $p=1, 2, 3, 4$. Solid line: exact solution; Red square: numerical solution.

5.2.4 Shock acoustic-wave interaction

The problem of shock-acoustic wave interaction [15] was solved to show the advantage of the present high-order limiter for the problems with both shock waves and complex smooth features. We solved the Euler equations (5.3) with a moving Mach=3 shock interacting with a sine wave in density, i.e., initially,

$$(\rho, p, v) = \begin{cases} (3.857143, 10.333333, 2.629369) & \text{for } x < -4, \\ (1 + 0.2\sin(5x), 1, 0) & \text{for } x \geq -4. \end{cases} \tag{5.4}$$

For comparison, a converged solution using a second-order MUSCL scheme on a grid of 3200 cells is used as the "exact" solution. In Fig. 18, the solution of density at $t=1.8$ is compared with the "exact" solution for $p=1, 2, 3$ with the present PFGM limiter on a medium mesh of $N=400$ cells and time step size $dt=0.0005$. It shows that the smooth local extrema are better recovered if using the present limiter in higher-order form ($p=2, 3$). A close-up view of the complex smooth region is also shown for each case in Fig. 18.

5.3 2D test cases

Next we test the present limiter for 2D inviscid flow problems with discontinuities. The conservative form of the 2D Euler equation can be written as

$$\frac{\partial Q}{\partial t} + \frac{\partial F}{\partial x} + \frac{\partial G}{\partial y} = 0, \tag{5.5}$$
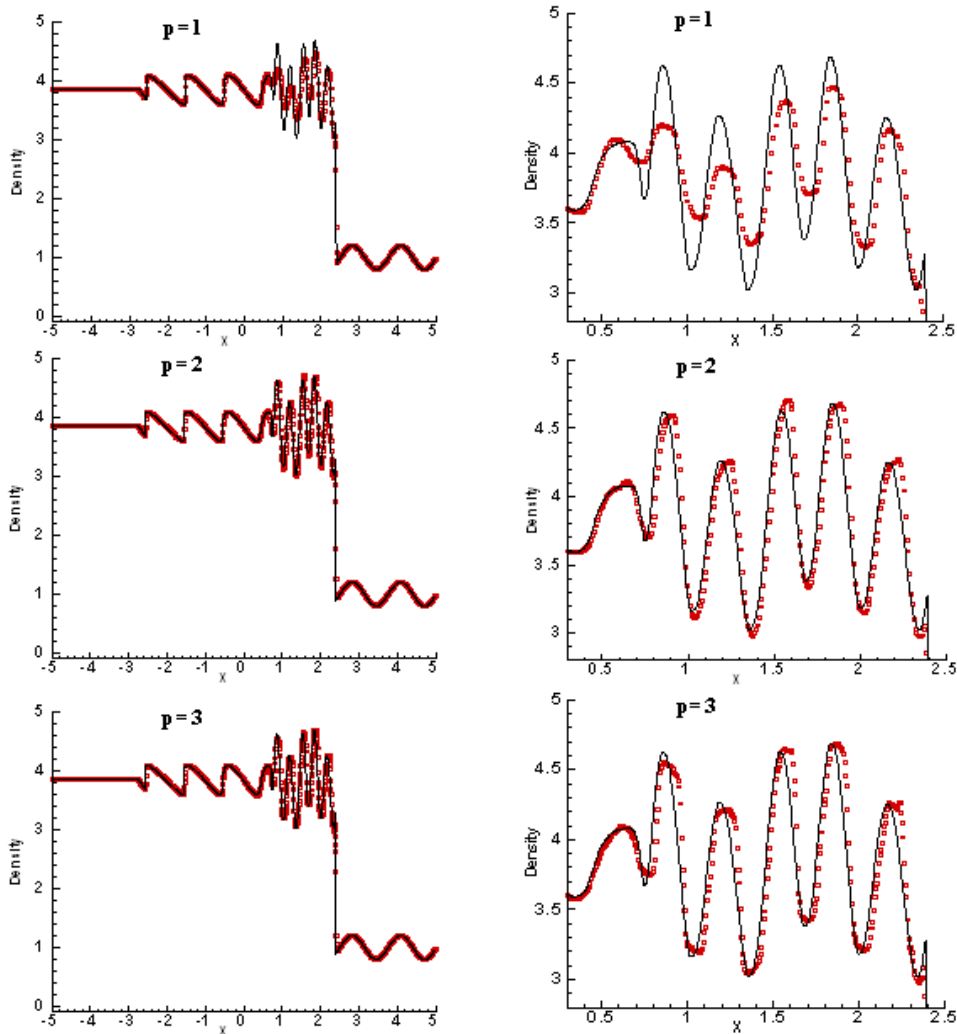
Figure 18: The shock-acoustic interaction problem, $t=1.8$, $N=400$ cells, $p=1$, 2, 3. Solid line: exact solution; red square: computed solution at the solution points. Right: close-up view for the complex smooth region in the left graphs.

where Q is the conservative solution variables, F, G are the inviscid flux given below,

$$Q = (\rho, \rho u, \rho v, E)^{\mathrm{T}}, \quad F = (\rho u, \rho u^2 + p, \rho uv, u(E + p))^{\mathrm{T}},$$
$$G = (\rho v, \rho uv, \rho v^2 + p, v(E + p))^{\mathrm{T}}.$$

Here ρ is the density, u, v are the velocity components in x and y directions, p is the pressure, and E is total energy. The pressure is related to the total energy by

$$E = \frac{p}{\gamma - 1} + \frac{1}{2}\rho(u^2 + v^2),$$

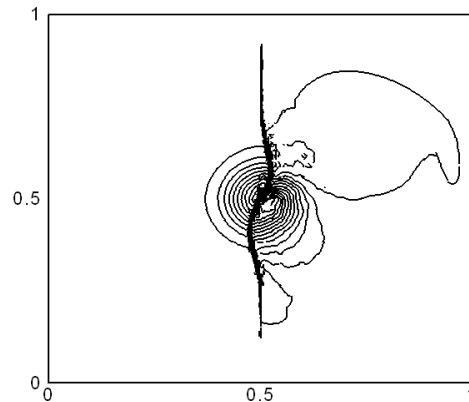with ratio of specific heat $\gamma = 1.4$.

Figure 19: Pressure contour for 2D shock-vortex interaction, t=0.2.

5.3.1 Shock vortex interaction

This problem describes the interaction between a stationary shock wave and a vortex, and is a good test for the PFGM in resolving both discontinuities and important smooth features. The flow conditions are the same as in [15]. The computational domain is taken to be $[0,2] \times [0,1]$. A stationary shock with a pre-shock Mach number of M_s=1.1 is positioned at x=0.5 and normal to the x-axis. Its left state is (ρ, u, v, p)=$(1, \sqrt{\gamma}, 0, 1)$. An isentropic vortex p/ρ^γ=const. is superposed to the flow left to the shock and centers at (x_c, y_c)=$(0.25, 0.5)$. Therefore the flow variables on the left side of the shock are as follows:

$$u = M_s \cdot \sqrt{\gamma} + \varepsilon \tau e^{\alpha(1-\tau^2)} \sin \theta, \qquad v = -\varepsilon \tau e^{\alpha(1-\tau^2)} \cos \theta,$$
$$\rho = \left(1 - \frac{\gamma-1}{4\alpha\gamma}\varepsilon^2 e^{2\alpha(1-\tau^2)}\right)^{\frac{1}{(\gamma-1)}}, \qquad p = \left(1 - \frac{\gamma-1}{4\alpha\gamma}\varepsilon^2 e^{2\alpha(1-\tau^2)}\right)^{\frac{\gamma}{(\gamma-1)}},$$

where

$$\tau = r/r_c \quad \text{and} \quad r = \sqrt{(x-x_c)^2 + (y-y_c)^2}.$$

Here ε denotes the strength of the vortex, α is the decay rate of the vortex; and r_c is the critical radius for which the vortex has the maximum strength. They are set to be ε=0.3, α=0.204, r_c=0.05.

The 3rd order SD scheme was employed in the simulation on a coarse mesh of 86×35 cells in order to have almost the same numbers of degree of freedom as in [15] (where the WENO method was used) for comparison purposes. The time step size used is dt=0.0005. The grids are uniform in y-direction and clustered near the shock in x-direction. The boundary conditions for the top and bottom boundaries are set to symmetry, or slip wall. The pressure contours computed with the present PFGM limiter and a linear limiter (in which the solution at the troubled cells is assumed linear) at t=0.05, t=0.20, and t=0.35 are shown in Figs. 20 and 21, respectively. It appears the present simulation captures the shock waves with a higher resolution than
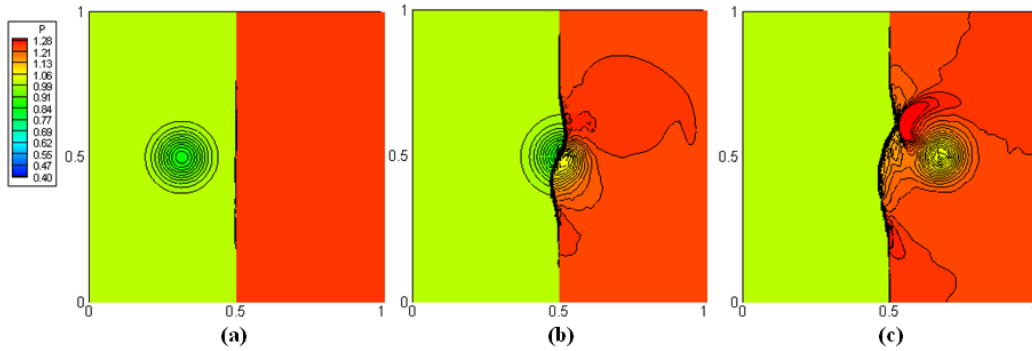
Figure 20: Pressure contours for the 2D shock-vortex interaction by the using 3rd-order PFGM limiter 61 contours from 0.4 1.29. (a) t=0.05; (b) t=0.2; (c) t=0.35.
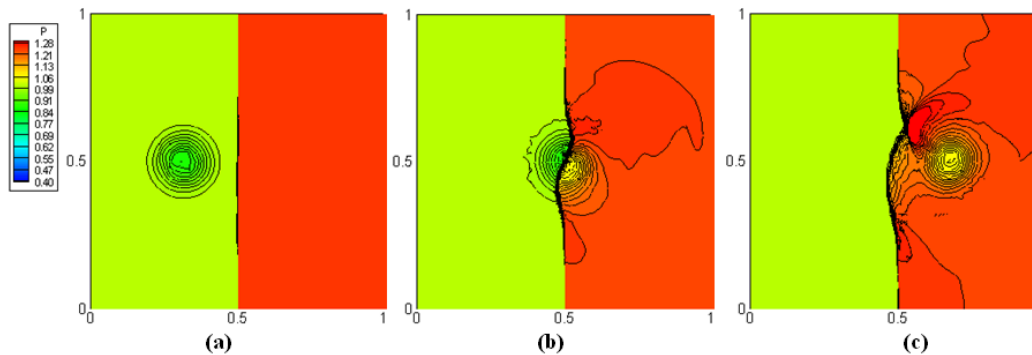

Figure 21: Pressure contours for the 2D shock-vortex interaction by the using linear limiter 61 contours from 0.4 1.29. (a) t=0.05; (b) t=0.2; (c) t=0.35.

[15], Fig. 15. The color plots clearly show the regions before and after the shock. A black and white contour plot is given in Fig. 19 (for t=0.2). Comparing Figs. 20 and 21, we can see that the PFGM limiter recovers the vortex much better than the linear limiter, and the shock discontinuity has been sharply captured as well by the present limiter.

Figs. 22 and 23 shows snapshots for later moments, t=0.6 and t=0.8 using the 3rd-order PFGM limiter and linear limiter, respectively. We can see here that the reflective boundary takes effects as time goes long enough when one of the shock bifurcations reaches the top boundary and is reflected. Fig. 22(b) shows that the reflection is well captured. Again the 3rd-order PFGM limiter gives better results than the linear limiter in terms of less numerical noise and better-resolved vortex.

5.3.2 Oblique shock reflection by a wedge

This example considers a Mach 2 flow passing a wedge of $20°$. Notice that in 5.3.1 the normal shock is aligned with the grid, while in this example we don't have this luxury. The state ahead of the shock is set to be $(\rho, u, v, P)=(1.4, 2, 0, 1)$. The boundary conditions are as follows: (1) supersonic inlet at the inlet on the left side; (2) inviscid wall boundary condition for the wall; (3) simple extrapolation boundary condition for
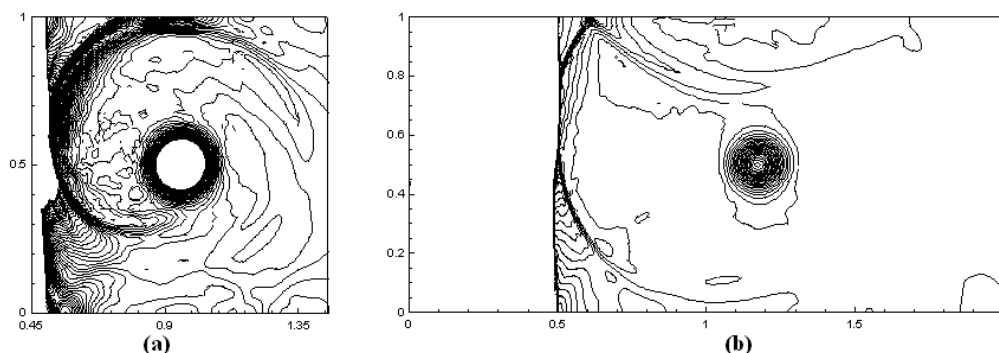
Figure 22: Pressure contours for the 2D shock-vortex interaction by the using 3rd-order PFGM limiter 90 contours from 1.19 1.37. (a) t=0.6; (b) t=0.8.
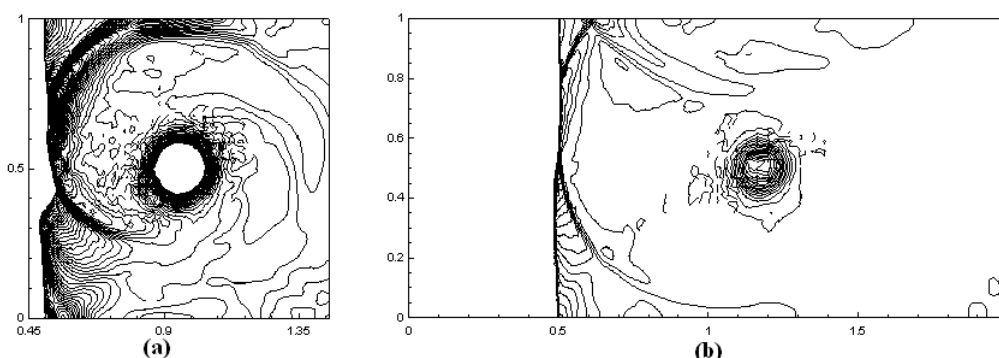

Figure 23: Pressure contours for the 2D shock-vortex interaction by the using linear limiter 90 contours from from 1.19 1.37. (a) t=0.6; (b) t=0.8.

the upper boundary and the outlet on the right end. A coarse mesh (400 elements, 20 boundary elements) was used for this case, as shown in Fig. 24(b). The density contours in Fig. 24(a) shows that the present 3rd-order PFGM limiter captured the shock sharply (within one element). Only the cells at the shock are marked (in red), and the typical marked cells when the shock is formed are shown in Fig. 24(b). As we can see, the AP-TVD marker works well as expected.

5.3.3 Transonic flow over NACA0012 airfoil

This example is the transonic flow over a NACA0012 airfoil at Mach 0.85 and an angle of attack α=1°, characterized by the existence of two shocks, one on the upper surface and one on the lower surface. To demonstrate the advantage of the present high-order limiter, we used a relatively coarse mesh (1584 hexahedral elements, 52 elements on the upper and lower wall surfaces) as shown in Fig. 25. An implicit LU-SGS scheme was used for time integration in this case.

Fig. 26(a) shows the Mach contours obtained with the 3rd-order PFGM limiter, and Fig. 26(b) gives a snapshot of the typical distribution of the marked cells. It is shown that the present limiter is indeed able to eliminate the spurious oscillations and capture the shock discontinuities sharply while maintaining the high-order accuracy
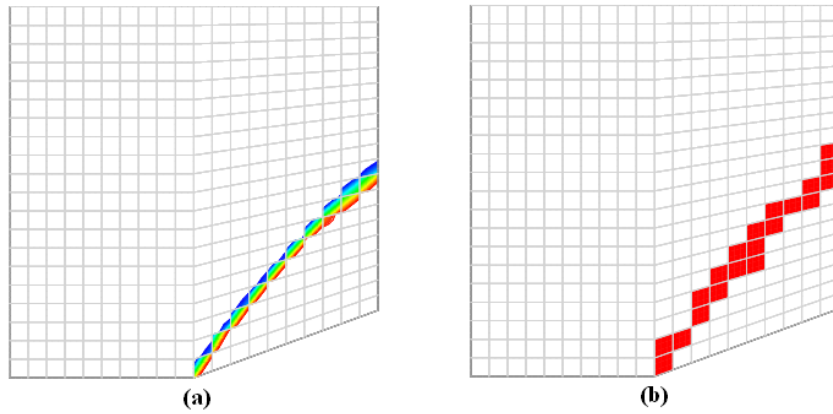
Figure 24: Mach 2 flow past a wedge of $20°$ by using the 3rd-order PFGM limiter with the SD method (400 elements, 20 boundary elements). (a) Density contour; (b) Marked cells.
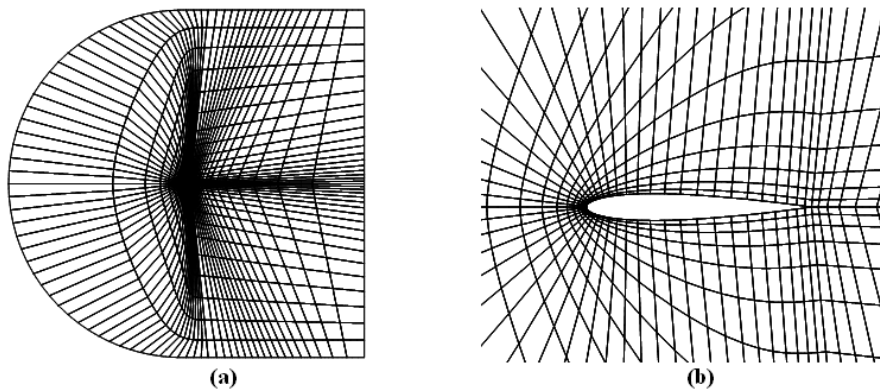

Figure 25: The unstructured hexahedral meshes for the NACA0012 airfoil in transonic flow (1584 elements, 52 wall boundary elements). (a) the whole domain; (b) close-up view around the airfoil.
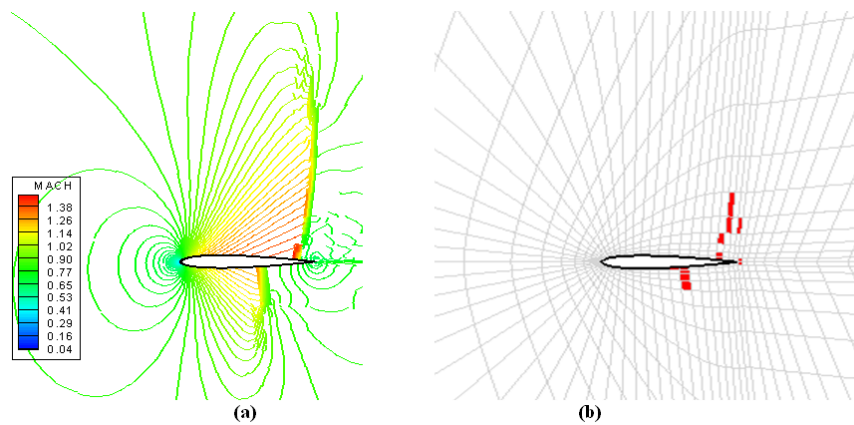

Figure 26: The transonic flow over NACA0012 airfoil (M_∞=0.85, α=1$°$) by using the 3rd-order PFGM limiter in the SD method. (a) Mach contours; (b) the marked cells (red) at the 1000th implicit time step.

at smooth regions. It was noticed that the marked cells are located just in the vicinity of the upper and lower shock discontinuities, and the average number of the marked cells during the LU-SGS implicit time iterations is a very small percentage (about 2%) of the total number of cells. Therefore it shows that the present AP-TVD marker works well and efficiently for multidimensional cases.

6 Conclusions

Three design criteria have been set for a general purpose limiter: (1) free of user-specified parameters, (2) capable of preserving a local degree p polynomial, (3) applicable to arbitrary unstructured meshes. The parameter-free generalized moment (PFGM) limiter developed in the present study appears to meet all of the criteria. The limiter is composed of two components: an efficient accuracy preserving TVD marker for "troubled cells" based on cell averaged state variables, and a hierarchical generalized moment limiter capable of handling arbitrary unstructured meshes. The PFGM limiter has been implemented and tested for a high-order SD method, although it can be easily applied to all other similar high-order methods. The AP-TVD marker is based on the cell-averaged solutions and solution derivatives, and is quite efficient to implement. It appears that smooth extrema are not marked, while the discontinuous cells are consistently marked, without the use of any user-specified parameter. The AP-TVD marker compares favorably against several markers in the literature, such as the TVB marker, KXRCF marker, or the Harten marker. Accuracy studies confirmed that the limiter is capable of preserving accuracy in smooth regions. Numerical tests for a wide variety of problems in 1D and 2D with both discontinuities and smooth features demonstrated the capability and usefulness of the PFGM limiter. A remaining challenge is to enhance the convergence property of the limiter for steady state problems.

Acknowledgments

References

[1] T. J. BARTH AND D. C. JESPERSON, *The design and application of upwind schemes on unstructured meshes*, AIAA Paper No. 89-0366, 1989.

[2] R. BISWAS, K. D. DEVINE AND J. FLAHERTY, *Parallel, adaptive finite element methods for conservation laws*, Appl. Numer. Math., 14 (1994), pp. 255–283.

[3] J. P. Boris and D. L. Book, *Flux corrected transport,1 SHASTA, a fluid transport algorithm that works*, J. Comput. Phys., 11 (1969), pp. 38–69.

[4] B. Cockburn, G. E. Karniadakis and C-W. Shu, *The development of discontinuous Galerkin methods*, Discontinuous Galerkin Methods, edited by B Cockburn, G. E. Karniadakis and C. W. Shu, Berlin: Springer, 2000.

[5] B. Cockburn and C-W. Shu, *TVB Runge-Kutta local projection discontinuous Galerkin finite element method for conservation laws II: general gramework*, Math. Comput., 52 (1989), pp. 411–435.

[6] A. W. Cook and W. H. Cabot, *A high-wavenumber viscosity for high resolution numerical method*, J. Comput. Phys., 195 (2004), pp. 594 -601.

[7] B. Fiorina and S. K. Lele, *An artificial nonlinear diffusivity method for supersonic reacting flows with shocks*, J. Comput. Phys., 222 (2007), pp. 246–264.

[8] S. K. Godunov, *A finite-difference method for the numerical computation of discontinuous solutions of the equations of fluid dynamics*, Mat. Sb. 47, 271 (1959).

[9] A. Harten, B. Engquist, S. Osher and S. Chakravarthy, *Uniformly high-order essentially non- oscillatory schemes III*, J. Comput. Phys., 71 (1987), pp. 231.

[10] A. Harten, *High resolution schemes for hyperbolic conservation laws*, J. Comput. Phys., 49 (1983), pp. 357–393.

[11] A. Harten, *ENO schemes with subcell resolution*, J. Comput. Phys., 83 (1989), pp. 148–184.

[12] H. T. Huynh, *A Flux Reconstruction Approach to High-Order Schemes Including Discontinuous Galerkin Methods*, AIAA-2007-4079, 18th AIAA Computational Fluid Dynamics Conference, June 2007, Miami, Florida.

[13] J. Jaffre, C. Johnson and A. Szepessy, *Convergence of the discontinuous Galerkin ?nite element method for hyperbolic conservation laws*, Models Methods Appl. Sci., 5 (1995), pp. 367–386.

[14] A. Jameson, W. Schmidt and E. Turkel, *Numerical simulation of the Euler equations by finite volume methods using Runge-Kutta time stepping schemes*, AIAA paper 81-1259, AIAA 5th Computations Fluid Dynamics Conference, 1981.

[15] G. Jiang and C-W. Shu, *Efficient implementation of weighted ENO schemes*, J. Comput. Phys., 126 (1996).

[16] D. A. Kopriva, *A staggered-grid multidomain spectral method for the compressible Navier-Stokes equations*, J. Comput. Phys., 143 (1998), pp. 125–148.

[17] D. A. Kopriva and J. H. Kolias, *A conservative staggered-grid Chebyshev multidomain method for compressible flows*, J. Comput. Phys., 125 (1996), pp. 244.

[18] L. Krivodonova, *Limiters for high-order discontinuous Galerkin methods*, J. Comput. Phys., 226 (2007), pp. 879–896.

[19] L. Krivodonova, J. Xin, J.-F. Remacle, N. Chevaugeon and J. E. Flaherty, *Shock detection and limiting with discontinuous Galerkin methods for hyperbolic conservation laws*, Appl. Numer. Math., 48 (2004), pp. 323–338.

[20] P. D. Lax and B. Wendroff, *Systems of conservation laws*, Comm. Pure Appl. Math., 13 (1960), pp. 217.

[21] M. S. Liou, *A sequel to AUSM: AUSM+*, J. Comput. Phys., 129 (1996).

[22] Y. Liu, M. Vinokur and Z. J. Wang, *Discontinuous spectral difference method for conservation laws on unstructured grids*, J. Comput. Phys., 216 (2006), pp. 780–801.

[23] Y. J. Liu, C-W. Shu, E. Tadmor and M. P. Zhang, *Central Discontinuous Galerkin methods on overlapping cells with a non-oscillatory hierarchical reconstruction*, SIAM J. Numer. Anal., 45 (2007), pp. 2442–2467.

[24] H. Luo, J. D. Baum and R. Lohner, *A Hermite WENO-based limiter for discontinuous*

Galerkin method on unstructured grids, J. Comput. Phys., 225 (2007), pp. 686–713.

[25] R. W. MACCORMACK AND B. S. BALDWIN, *A numerical method for solving the Navier-Stokes equations with application to shock-boundary layer interaction*, AIAA 75-1.

[26] P.-O. PERSSON AND J. PERAIRE, *Sub-cell shock capturing for discontinuous Galerkin methods*, AIAA-2006-112, 2006.

[27] J. QIU AND C-W. SHU, *A comparison of troubled-cell indicators for Runge-Kutta discontinuous Galerkin Methods using weighted essentially nonoscillatory limiters*, SIAM J. Sci. Comput., 27 (2005).

[28] J. QIU AND C-W. SHU, *Runge-Kutta discontinuous Galerkin method using WENO limiters*, SIAM J. Sci. Comput., 26 (2005), pp. 907–929.

[29] J. QIU AND C-W. SHU, *Hermite WENO schemes and their application as limiters for Runge-Kutta discontinuous Galerkin method: one-dimensional case*, J. Comput. Phys., 193 (2003), pp. 115–135.

[30] W. H. REED AND T. R. HILL, *Triangular mesh methods for the neutron transport equation*, Technical report LA-UR-73-479, Los Alamos Scientific Laboratory, 1973.

[31] P. L. ROE, *Approximate Riemann solvers, parameter vectors, and difference schemes*, J. Comput. Phys., 43 (1981), pp. 357–372.

[32] C-W. SHU, *Total-variation-diminishing time discretizations*, SIAM J. Sci. Stat. Comput., 9 (1988), pp. 1073–1084.

[33] C-W. SHU AND S. OSHER, *Efficient implementation of essentially non-oscillatory shock-capturing schemes*, J. Comput. Phy., 77 (1998), pp. 439-471.

[34] Y. SUN, Z. J. WANG AND Y. LIU, *High-order multidomain spectral difference method for the Navier-Stokes equations*, AIAA-2006-0301.

[35] Y. SUN, Z. J. WANG AND Y. LIU, *Efficient implicit non-linear LU-SGS approach for compressible flow computation using high-order spectral difference method*, Commun. Comput. Phys., 5 (2009), pp. 760–778.

[36] E. TADMOR, *Convergence of spectral methods for nonlinear conservation laws*, SIAM J. Numer. Anal., 26 (1989), pp. 30.

[37] K. VAN DEN ABEELE, C. LACOR AND Z. J. WANG, *On the stability and accuracy of the spectral difference method*, J. Sci Comput., 37 (2008), pp. 162–188.

[38] B. VAN LEER, *Towards the ultimate conservative difference scheme II. Monotonicity and conservation combined in a second-order scheme*, J. Comput. Phys., 14 (1974), pp. 361.

[39] B. VAN LEER, *Towards the ultimate conservative difference scheme V. a second order sequel to Godunov's method*, J. Comput. Phys., 32 (1979), pp. 101–136.

[40] J. VON NEUMANN AND R. D. RICHTMYER, *A method for the numerical calculations of hydrodynamical shocks*, J. Math. Phys., 21 (1950), pp. .

[41] Z. J. WANG, *Spectral (Finite) volume method for conservation laws on unstructured grids: Basic formulation*, J. Comput. Phys., 178 (2002), pp. 210–251.

[42] Z. J. WANG AND Y. LIU, *Spectral (finite) volume method for conservation laws on unstructured grids II: extension to two-dimensional scalar equation*, J. Comput. Phys., 179 (2002), pp. 665.

[43] Z. J. WANG, *High-order methods for the euler and Navier-Stokes equations on unstructured grids*, Progress in Aerospace Science, 43, (2007), pp. 1-41.

[44] H. C. YEE, R. F. WARMING AND A. HARTEN, *Implicit TVD schemes for steady-state calculations*, J. Comput. Phys., 57 (1985), pp. 327–360.

[45] S. YOON AND A. JAMESON, *Lower-upper symmetric-Gauss-Seidel method for the Euler and Navier-Stokes equations*, AIAA Journal, 26 (1988), pp. 1025–1026.